AIP | Physics of Fluids

Stratified shear flow instabilities at large Richardson numbers

Alexandros Alexakis

Citation: Phys. Fluids **21**, 054108 (2009); doi: 10.1063/1.3147934
View online: http://dx.doi.org/10.1063/1.3147934
View Table of Contents: http://pof.aip.org/resource/1/PHFLE6/v21/i5
Published by the American Institute of Physics.

Related Articles

The impulse response of a high-speed jet forced with localized arc filament plasma actuators
Phys. Fluids 24, 125104 (2012)

Trapped disturbances and finite amplitude downstream wavetrains on the f-plane
Phys. Fluids 24, 106601 (2012)

Floating extensional flows
Phys. Fluids 24, 091111 (2012)

Separated shear layer transition over an airfoil at a low Reynolds number
Phys. Fluids 24, 084105 (2012)

Counterpropagating Rossby waves in confined plane wakes
Phys. Fluids 24, 074102 (2012)

Additional information on Phys. Fluids

Journal Homepage: http://pof.aip.org/
Journal Information: http://pof.aip.org/about/about_the_journal
Top downloads: http://pof.aip.org/features/most_downloaded
Information for Authors: http://pof.aip.org/authors

ADVERTISEMENT

Downloaded 22 Jan 2013 to 129.199.120.226. Redistribution subject to AIP license or copyright; see http://pof.aip.org/about/rights_and_permissions

Stratified shear flow instabilities at large Richardson numbers

Alexandros Alexakis[a)]
Laboratoire de Physique Statistique, Ecole Normale Superieure, rue Lhomond, 75231 Paris, France

(Received 9 January 2009; accepted 5 May 2009; published online 29 May 2009)

Numerical simulations of stratified shear flow instabilities are performed in two dimensions in the Boussinesq limit. The density variation length scale is chosen to be four times smaller than the velocity variation length scale so that Holmboe or Kelvin–Helmholtz unstable modes are present depending on the choice of the global Richardson number Ri. Three different values of Ri were examined Ri=0.2, 2, and 20. The flows for the three examined values are all unstable due to different modes, namely: the Kelvin–Helmholtz mode for Ri=0.2, the first Holmboe mode for Ri=2, and the second Holmboe mode for Ri=20 that has been discovered recently and this is the first time that it is examined in the nonlinear stage. It is found that the amplitude of the velocity perturbation of the second Holmboe mode at the nonlinear stage is smaller but comparable to first Holmboe mode. The increase in the potential energy, however, due to the second Holmboe modes is greater than that of the first mode. The Kelvin–Helmholtz mode is larger by two orders of magnitude in kinetic energy than the Holmboe modes and about ten times larger in potential energy than the Holmboe modes. The effect of increasing Prandtl number is also investigated, and a weak dependence on the Prandtl number is observed. The results in this paper suggest that although mixing is suppressed at large Richardson numbers it is not negligible, and turbulent mixing processes in strongly stratified environments cannot be excluded. © *2009 American Institute of Physics*. [DOI: 10.1063/1.3147934]

I. INTRODUCTION

The destabilization of stratified layer due to the influence of a shear is a common phenomenon in nature. It occurs when the pressure gradients in the flow can overcome gravity and overturn the fluid. If the Reynolds number is large enough then this process quickly becomes turbulent, diffusion is enhanced by the generation of small scales and the kinetic energy of the flow is converted irreversibly to potential energy. The rate kinetic energy is converted to potential energy and the total amount of potential energy gained can be of crucial importance in determining the evolution of many physically important systems, like the atmosphere,[1,2] oceanic,[3–6] and astrophysical flows.[7–9] In particular in this work the generation of turbulence and mixing in strongly stratified environments is examined. Such flows appear in accretion flows of hydrogen and helium into compact stellar object (white dwarf) composed of carbon and oxygen.[7,8] A detailed analysis of the nuclear reactions of hydrogen burning has shown that energy release via catalytic nuclear reactions in which carbon and oxygen play a crucial role can lead to a nuclear runaway, in which a large fraction of the accreted matter is expelled in the form of a shell; such a runway is referred in the astronomical literature as a nova. However, how the needed carbon and oxygen of the compact star is mixed to the overlying accreted envelope in an environment where the acceleration of gravity can six orders of magnitude larger than terrestrial values (Ri$\sim$1–100 depending on the shear generation mechanism[7]) is still an open question. Turbulent mixing in the presence of strong stratification is also reported in atmospheric and oceanic flows.[10–12] It is of interest therefore to be able to estimate the amount of mass mixed and how much increase of the potential energy can be generated by shear flow instabilities as a function of the control parameters of the system. To that respect simple shear layer models of velocity shear profiles $U(y)$ and density profiles $\rho(y)$ that depend only on the vertical coordinate of the system (here taken to be y) have been proven very useful in understanding the involved processes.

This work investigates a model first introduced by Hazel.[13] The model assumes a velocity profile given by

$$U_H(y) = U_0 \tanh(y/L_U) \tag{1}$$

and the density profile given by

$$\rho_H(y) = \rho_0[1 - \epsilon \tanh(y/L_\rho)], \tag{2}$$

that are illustrated in Fig. 1. The ratio of the velocity variation length scale L_U to the density variation length scale $R=L_U/L_\rho$ is one of the control parameters of the system. Another important control parameter in this system is the Richardson number that expresses the ratio of the stabilizing effect of gravity to the destabilizing effect of the shear. For a general velocity and density profile the Richardson number can be defined locally at a height y as

$$\mathrm{Ri}_{\mathrm{loc}}(y) = -g\frac{d\rho}{dy}/\rho\left(\frac{dU}{dy}\right)^2,$$

where g is the acceleration of gravity. It also convenient to define a global Richardson number Ri in order to give a general measure of the strength of the stratification. In this work Ri is going to be defined as the local Richardson

[a)]Electronic mail: aalexakis@gmail.com.

 © 2009 American Institute of Physics

Downloaded 22 Jan 2013 to 129.199.120.226. Redistribution subject to AIP license or copyright; see http://pof.aip.org/about/rights_and_permissions

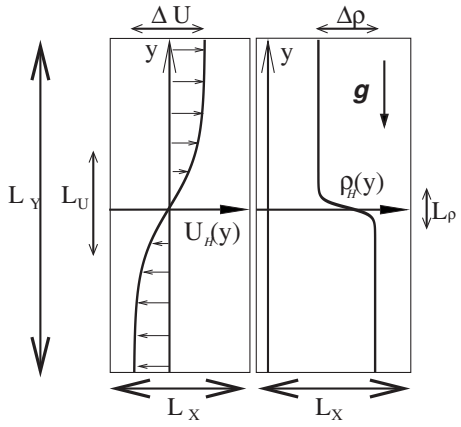

FIG. 1. A sketch of the model under study.

number at $y=0$, that for the Hazel model becomes $\mathrm{Ri} \equiv \mathrm{Ri}_{\mathrm{loc}}(0) = g\epsilon R L_U / U_0^2$.

Instabilities and generation of turbulence at large values Richardson numbers seem somehow prohibited since the Miles–Howard theorem[14] guarantees that any flow in the inviscid nondiffusive limit is linearly asymptotically stable if the local Richardson number is everywhere smaller than 1/4. This has restricted a lot of investigations to small values of global Richardson numbers. However, depending on the details of the flow and the density stratification, there can be regions in space where the local Richardson number can be smaller than 1/4 while the global Richardson number is larger than 1/4. These flows cannot be excluded from becoming unstable.

For the Hazel model if R is smaller than $\sqrt{2}$ the $\mathrm{Ri}_{\mathrm{loc}}(y)$ has a unique minimum at $y=0$ thus, linear instability can exist only if the global Richardson number is smaller than 1/4. The unstable modes in this case are stationary (nondispersive) waves concentrated around the $y=0$ plane where the flow has the strongest shear. These modes are referred in the literature as Kelvin–Helmholtz modes (KH-modes) due to their resemblance with the instability of step function density and velocity profile investigated by Lord Kelvin[15] and Helmholtz.[16] The linear stability of these modes has been investigated analytically by Miles[17] and numerically by Hazel.[13] The nonlinear development of Kelvin–Helmholtz unstable modes has been investigated extensively in the literature both experimentally[18,19] and numerically.[20–26] Their nonlinear evolution leads to the formation of discrete billows around the height of the strongest shear that curl the density gradients. Secondary three dimensional instabilities at the nonlinear stage lead to the formation of a turbulent layer and fast mixing.[27]

For R in the range $\sqrt{2} < R < 2$ the local Richardson number $\mathrm{Ri}_{\mathrm{loc}}(y)$ has two minima symmetrically placed around the origin with values smaller than the global Richardson number. However in this range of R instability has been found only for values of the global Richardson number smaller than 1/4 with similar nonlinear evolution as with the $R < \sqrt{2}$ case.

For R larger than 2, $\mathrm{Ri}_{\mathrm{loc}}(y)$ decays exponentially to 0 for large values of y. Thus, the Miles–Howard theorem cannot guarantee linear stability of the flow even for arbitrarily large values of the global Richardson number. The parameter range $R > 2$ therefore appears to be a good candidate for instabilities in the strongly stratified limit. A numerical investigation of the inviscid linear instability problem in this parameter range was first performed by Hazel[13] (and later on by Smyth and Peltier[28]). These early investigations have shown that beside the Kelvin–Helmholtz instability that is confined to values of the global Richardson number smaller than 1/4, new unstable modes are present. These new modes appear as pairs of counterpropagating dispersive waves that are concentrated above and bellow the density "interface." The unstable modes were found to be confined in a strip (in the Ri-wavenumber plane) that extends to arbitrarily large values of Ri. These results reproduce qualitatively the results of a piece wise linear velocity and discontinuous density profile introduced earlier by Holmboe[29] and are referred in literature as Holmboe modes. Numerical investigations of the Holmboe instability have been performed in two[30] and three dimensions.[31–36] It is worth noting that in Ref. 33 it was found that the Holmboe mode for $R=3$ resulted in larger irreversible increase of potential energy than the Kelvin–Helmholtz mode with $R=1$ although the latter one had larger growth rate. Experimentally Holmboe modes have been investigated by various groups.[37–44] In the nonlinear stage the unstable waves form of cusps, whose breaking is responsible for mixing.

The persistence of the Holmboe instability at arbitrary large values of Ri makes them better candidates for the generation of turbulence at strongly stratified environments. However, the growth rate of the unstable modes appears to decrease exponentially with the Richardson number,[29] and the presence of even small viscosity restricts the region of instability to relatively small values of Ri.

Recently it was shown by the author[45,46] that the unstable modes found by Hazel[13] are not the only ones present in the Hazel model. When $R > 2$ there is an infinite series of unstable regions in the Richardson-wavenumber parameter space in the form of strips. Each new instability strip appears at larger value of Ri and corresponds to a different internal gravity wave that becomes unstable when its phase speed becomes equal to the maximum velocity of the flow.[46] These modes are going to be referred to as higher Holmboe modes, and are going to be numbered with the order of appearance as Ri is increased (first Holmboe mode, second Holmboe mode, etc.) with the mode found by Hazel[13] and Smyth and Peltier[28] being the first Holmboe mode. It was further found in Ref. 45 that for a fixed Ri the highest Holmboe mode, has the largest growth rate. Therefore these newly discovered modes may provide a new mechanism for generation of turbulence and mixing in strongly stratified flows.

The nonlinear evolution of the higher Holmboe modes, has not been investigated in the nonlinear regime neither numerically nor experimentally since typical investigations so far have focused on small values of the global Richardson number. The results of the linear theory for the higher Holmboe modes are promising for the generation of turbulence in strongly stratified environments, however, turbulence and mixing can only be addressed in the nonlinear stage of the evolution.

Downloaded 22 Jan 2013 to 129.199.120.226. Redistribution subject to AIP license or copyright; see http://pof.aip.org/about/rights_and_permissions

This work examines the development of shear flow instabilities that span three orders of magnitude of the global Richardson number. The examined values Ri=0.2, Ri=2.0, and Ri=20, correspond to the three different unstable modes: the Kelvin–Helmholtz mode for Ri=0.2, the first Holmboe mode for Ri=2.0 and the second Holmboe mode for Ri=20. Since this is the first numerical study of the second Holmboe mode the investigation is restricted only to two dimensions, in order to get a basic understanding of the nonlinear development without the additional complications of secondary three dimensional instabilities. However, since properties of turbulence and mixing can be very different in three and two dimensions care is needed in the interpretation of the results, and their implications to the physical systems. For this reason the results in this paper will be restricted only to basic mechanisms involved and the relative increase of kinetic and potential energy of the examined modes without examining in detail mixing properties that would depend on the dimensionality of the system.

In Sec. II we introduce in detail the model that is going to be investigated, examine the linear theory of the viscous problem, give the details of the numerical code, and justify the choice of parameters. Section III presents the results of the numerical simulations. The last section discusses the results of this work and their implications and conclusions are drawn.

II. METHODOLOGY

A. The mathematical model

In this study a two dimensional incompressible flow of an inhomogeneous in density fluid will be considered. The fluid is confined in a rectangular box of size L_Y, L_X with periodic boundary conditions in the x-direction and free-slip ($u_y=0$, $\partial_y u_x=0$), no-flux ($\partial_y \rho=0$) conditions in the top and bottom boundary. The Boussinesq equations for the evolution of the velocity and density field then read

$$\partial_t \mathbf{u} + \mathbf{u}\cdot\nabla\mathbf{u} = \frac{1}{\rho_0}\nabla P - \mathbf{j}g\frac{\rho}{\rho_0} + \nu\nabla^2\mathbf{u} + \mathbf{i}F, \tag{3}$$

$$\partial_t \rho + \mathbf{u}\cdot\nabla\rho = \kappa\nabla^2\rho + S, \tag{4}$$

where $\mathbf{u}$ is the incompressible velocity field, and ρ is the field of the density variation. The mean value of the density field is given by ρ_0. ν and κ are the viscosity and the diffusivity of the fluid. g is the acceleration of gravity assumed here to act in the negative y-direction. $F(y)$ is a forcing function and $S(y)$ is density source/sink term with zero average so that the space averaged density $\langle\rho\rangle=\rho_0$ is conserved. F and S are chosen so that $F=-\nu\partial_y^2 U_H$ and $S=-\kappa\partial_y^2\rho_H$ where $U_H(y)$ and $\rho_H(y)$ are given in Eqs. (1) and (2) with $y=0$ corresponding to the midplane of our box. With this choice $\mathbf{u}=\mathbf{i}U_H(y)$ and $\rho=\rho_H(y)$ are exact solutions of the Boussinesq equations (3) and (4). {To be more exact we need to add an exponentially small term in Eqs. (1) and (2) [proportional to $-2U_0 y/L_y \operatorname{sech}^2(L_Y/2L_U)$, and $-2\rho_0 y/L_Y \operatorname{sech}^2(RL_Y/2L_U)$] in order for the laminar solutions $U_H(y)$ and $\rho_H(y)$ to satisfy the boundary conditions. This term was included in the numerical simulations for consistency although at the examined box sizes presented here it did not seem to play an important role, however, at smaller box sizes it helped to avoid the formation of boundary layers at $y=\pm L_Y/2$.} A sketch of the model that is investigated is shown in Fig. 1.

To nondimensionalize the system we are going to use the velocity amplitude U_0, the velocity length scale L_U, and the density ρ_0. Thus, in the results presented in Sec. III all length scales are in units of L_U, time scales in units of L_U/U_0, and energy density in units of $\rho_0 U_0^2$. This leads to four nondimensional control parameters that control the Hazel model, namely: the Richardson number Ri defined as $\mathrm{Ri}\equiv\mathrm{Ri}_{\mathrm{loc}}(0)=g\epsilon L_U^2/U_0^2 L_\rho$, the Reynolds number $\mathrm{Re}\equiv U_0 L_U/\nu$, the Prandtl (or Schmidt) number $\mathrm{Pr}\equiv\nu/\kappa$ and the ratio of the velocity length scale to the density length scale $R=L_U/L_\rho$. In addition to the just mentioned parameters of the Hazel model there are two more parameters in the examined system due to the finite size of the computational box $\ell_Y\equiv L_Y/L_U$ and $\ell_X\equiv L_X/L_U$.

B. The linear instability problem

Before investigating the nonlinear problem we need to examine the linear stability problem for the diffusive and dissipative system in parameter range that is going to be examined with the numerical simulations. The linear stability theory considers the evolution of infinitesimal perturbations to the background density and velocity profiles. The velocity perturbation is going to be written in terms of a stream function ψ as $\mathbf{u}-\mathbf{i}U_H(y)=\mathbf{i}\partial_y\psi-\mathbf{j}\partial_x\psi$ and the density perturbation as $\rho-\rho_H=\theta$. A normal mode expansion will be assumed

$$\psi=\sum\tilde{\psi}_k e^{ik(x-ct)},\quad \theta=\sum\tilde{\theta}_k e^{ik(x-ct)},$$

with k being the wave number in the x-direction and c the complex phase speed. If the imaginary part of c is greater than zero then the normal mode will grow exponentially with growth rate $\gamma=k\Im(c)$ [where $\Im()$ stands for imaginary part]. Linearizing Eqs. (3) and (4) with respect to ψ and θ lead to the eigenvalue problem

$$\begin{aligned}&\left[(U_H-c)D^2-U_H''-\frac{\nu}{ik}(D^2)^2\right]\tilde{\psi}_k+\left[\frac{g}{\rho_0}\right]\tilde{\theta}_k=0,\\&\left[(U_H-c)-\frac{\kappa}{ik}D^2\right]\tilde{\theta}_k+\rho_H'\tilde{\psi}_k=0\end{aligned} \tag{5}$$

for the eigenvalue c. Here, prime indicates differentiation with respect to the y-coordinate and D^2 stands for the operator $D^2=\partial_y^2-k^2$. If we assume zero viscosity and diffusivity Eq. (5) simplifies to the Taylor–Goldstein equation (see, for example, Ref. 47).

In this work, however, the effect of viscosity and diffusivity cannot be neglected and the full eigenvalue problem (5) needs to be examined. The eigenvalue problem was solved numerically by expanding the two perturbative fields ψ_k, θ_k in a finite sum of sines (stream function) and cosines (density). With this choice the two fields always satisfy the boundary conditions. The eigenvalue problem (5) then becomes a matrix eigenvalue problem of the form $Ax=cBx$ which is then solved using the linear algebra package LAPAC.

Downloaded 22 Jan 2013 to 129.199.120.226. Redistribution subject to AIP license or copyright; see http://pof.aip.org/about/rights_and_permissions

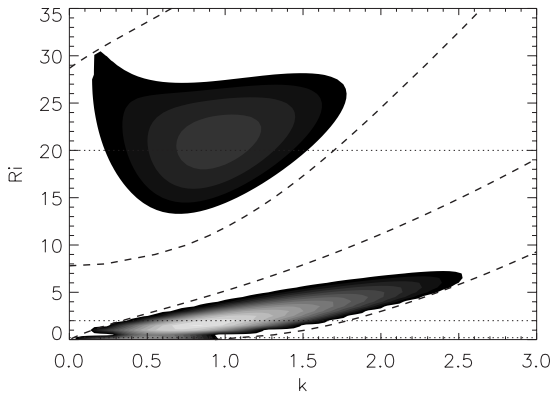

FIG. 2. The stability diagram in the Richardson-wavenumber plane. Shaded regions show the locations of positive growth rate (light regions correspond to high growth rate), white regions are stable. The dashed lines indicate the stability boundaries of the inviscid, nondiffusive system. The dotted horizontal lines indicate the three examined Richardson numbers.

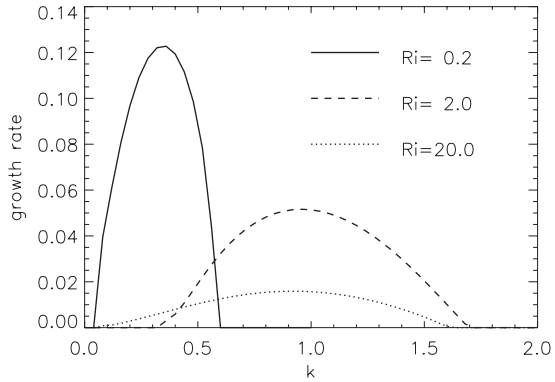

FIG. 3. The growth rate for the three examined values of the Richardson number: Ri=0.2 Kelvin–Helmholtz. Solid line Ri=2.0 first Holmboe mode dashed line, Ri=20, second Holmboe mode.

For Re=500 and $R=4$ that will be the choice in the numerical simulations presented here, 128 modes were sufficient for the code to converge to the third digit of the growth rate for all the modes except the ones close to the stability boundaries. For the modes with the real part of c close to ± 1 (that correspond to the small wave number boundary of Holmboe instability) the eigenvalue code had problem converging with such accuracy. The results in this paper are restricted modes with $|c|<0.98$ and as a result the stability boundaries presented here extend to slightly smaller wavenumbers.

Figure 2 displays the stability diagram in the Richardson-wavenumber plane for Re=500, $R=4$, Pr=1, and $\ell_Y=8\pi$. Shaded regions show the locations of positive growth rate (light regions correspond to high growth rate). Different regions of instability can be seen. The shaded region for large Richardson numbers ($12 \lesssim \mathrm{Ri} \lesssim 30$) corresponds to the second Holmboe mode, while the shaded region for smaller values of $\mathrm{Ri} \lesssim 8$ corresponds to the first Holmboe mode. The Kelvin–Helmholtz modes are restricted to small values of $\mathrm{Ri}<0.25$ and cannot be seen clearly in this diagram. The Kelvin–Helmholtz instability region appears as a thin shaded region close to Ri=0 in the range $0<k<1$. The dashed lines indicate the stability boundaries of the inviscid, nondiffusive system. It can be clearly seen that even a small viscosity (Re=500) has significantly reduced the unstable regions.

Figure 3 shows the growth rates at the same parameter regime as a function of the wave number for the three examined values of the Richardson number Ri. As can be seen the Kelvin–Helmholtz mode has the largest growth rate (solid line) $\gamma \simeq 0.127$ for $k \simeq 0.36$, the first Holmboe mode (dashed line) has maximum growth rate $\gamma \simeq 0.0516$ for $k \simeq 0.96$, and finally the second Holmboe mode has maximum growth rate $\gamma \simeq 0.0159$ for $k \simeq 0.92$. It is worth noting when comparing the Kelvin–Helmholtz modes with the second Holmboe mode that although the Richardson number has changed by a factor of 100 the growth rate has been decreased by a factor less than 10.

Different values of Re have also been examined. Here, it is just noted that unstable second Holmboe modes were found for Reynolds numbers $\mathrm{Re} \gtrsim 160$. The maximum growth rate for the second Holmboe mode at $\mathrm{Ri} \simeq 22$, $k \simeq 1$ becomes roughly Reynolds number independent when $\mathrm{Re} \gtrsim 500$ (a difference less than 5% was noted for the growth rate for Re=500 and Re=1000).

C. The numerical method

To solve Eqs. (3) and (4) a psedospectral code was used. The velocity field was written in terms a stream function ψ as $\mathbf{u}=\mathbf{i}\partial_y\psi-\mathbf{j}\partial_x\psi$. The stream function and the density field were expanded in sines and cosine modes (respectively) in the y-direction and in Fourier modes in the x-direction.

$$\psi=\sum_{\mathbf{k}} \tilde{\psi}_{\mathbf{k}} e^{ik_x x} \sin(k_y y'), \quad \rho=\sum_{\mathbf{k}} \tilde{\rho}_{\mathbf{k}} e^{ik_x x} \cos(k_y y'),$$

where $y'=y-\ell_Y/2$ and $k_x=2\pi n/\ell_X$, $k_y=\pi m/\ell_Y$ with n, m integers. The spatial derivatives were calculated in sine-Fourier space while products of fields were calculated in real space. Dialiasing was achieved using the 2/3 rule. The fields were advanced in time using a third order Runge–Kutta method.

The adopted resolution for each performed run was decided based on the spectral properties of the two fields. A run was considered well resolved if the gradients of the two advected quantities density ρ and vorticity $w=\nabla\times\mathbf{u}$ were sufficiently resolved so that the peak of the spectrum of $\nabla\rho$ and ∇w larger (roughly by a factor of 10) than its value at the largest wave number.

Special care needs to be taken to determine the time step that satisfies the Courant–Friedrichs–Lewy (CFL) criterion.[48] The time step Δt used in the code should be smaller than the grid size Δx divided by the maximum speed in the problem. There are two relevant speeds in the examined problem one given by the flow velocity and one given by the gravity wave speed. For sufficiently sharp density interfaces the gravity phase speed scales like $c \sim \sqrt{g/k}$. Typically in simulations of the Kelvin–Helmholtz or the first Holmboe mode the criterion $\Delta t > \Delta x/U_0$ is sufficient to satisfy CFL since U_0 is the largest speed in the system. (Note that the phase speed of the unstable Holmboe modes has to be with in the range of U for the instability to exist.) An exception to this rule is the case

Downloaded 22 Jan 2013 to 129.199.120.226. Redistribution subject to AIP license or copyright; see http://pof.aip.org/about/rights_and_permissions

for which boxes much larger ($L_x \gg L_U$) than the typical unstable wavelength are considered. For such long boxes, gravity waves of much larger wavelengths, and thus much larger phase speeds are allowed in the computational box. In this case it is the phase speed of the longest (and thus fastest) gravity wave that determines the allowed time step.

When investigating the second Holmboe mode one needs to be more careful because the unstable gravity wave mode is not the fastest mode in the system but rather the first Holmboe mode which is stable and has phase speed much larger than U_0. As a result a much smaller time step was used for the simulations of the second Holmboe mode. In practice the time step used was based on the formula $\Delta t = a\Delta x / \max(U_0, \sqrt{gL_X/2\pi})$ for $a=0.1$.

D. Parameter choice

In principle it is desirable to study this system in the limit $\mathrm{Re}, \ell_X, \ell_Y \to \infty$ in order to make contact with flows that appear in nature. In addition large numbers of $\mathrm{Ri} \gg 1$ should be considered for the astrophysical flows that were mentioned in Sec. I. The Prandtl number also is expected to be large to justify the presence of the sharp interface. Furthermore, in nature, the instabilities develop both in space and time. Spatial evolution can then influence the behavior of the modes as has been shown in Refs. 49 and 50. Ideally then, the spatial evolution of a localized perturbation in a long computational domain should also be considered. However, computational constraints put strong restrictions on the parameter space that can be examined.

In the present investigation, R was fixed to the value $R=4$ that is sufficiently larger than the critical value $R=2$ but not too large so that the density interface is too sharp to resolve. The three examined values of the Richardson number $\mathrm{Ri}=0.2$, 2, and 20 were based on the results of the linear theory. Both for the first and the second Holmboe mode the values of $\mathrm{Ri}=2$ and $\mathrm{Ri}=20$ are very close to the value for which the growth rate obtains its maximum value in the Ri-k plane for each mode (as can be seen in Fig. 2). For the Kelvin–Helmholtz mode we could have chosen a value of Ri that is arbitrarily small, since the maximum growth rate is obtained for $\mathrm{Ri}=0$. The choice of $\mathrm{Ri}=0.2$ was made so that the three values differ by an order of magnitude each.

The choice for ℓ_x was based on resolution and time step restrictions. As mentioned in the previous section increasing ℓ_x not only increases the number of modes that are needed for a fixed resolution but also decreases the time step. Two choices were made for this parameter. First single mode perturbations were examined and ℓ_x was fixed to the value $\ell_x = 2\pi$ for the Holmboe modes so that the evolution of the most unstable wavenumber $k \simeq 1$ is captured. Similarly for the Kelvin–Helmholtz instability the choice of $\ell_x = 8\pi$ was made. For a second set of runs that more than single wavelengths was perturbed the choice $\ell_x = 8\pi$ was made for all three values of the examined Richardson numbers so that also subharmonic coupling can also be captured. The evolution of a localized disturbance in time and space (see Refs. 49 and 50) would require much larger values of ℓ_x and is not considered here. ℓ_y has to be sufficiently large so that the boundaries play minimal role in the development of the instability. In the simulations the value $\ell_Y = 8\pi$ was chosen. It proved to be sufficient for all modes.

The Reynolds number was based on resolution requirements. In the examined cases a uniform grid with 512 grid points in the y-direction proved to be sufficient to resolve flows with $\mathrm{Re}=500$. Larger runs of 1028 grid points in the y-direction with the same Reynolds number were also performed but for shorter times that were in very good agreement with the 512 runs.

The choice of the Prandtl (Schmidt) number $\mathrm{Pr}=1$ was also based on resolution requirements. In most cases that Holmboe instability appears are with Pr much larger than one. However such a choice would require an even finer grid to resolve the resulting thin filaments of density gradients. In Ref. 34 different grid sizes were considered for the evolution of the velocity and the density field so that large Prandtl can be considered efficiently. Such an option will be considered in future investigations. To test the dependence of the results on the Prandtl number a parameter study is performed varying the Prandtl number from 1 to 10.

At this point, the choice of including the density source and forcing functions S, F should also be justified. For sufficiently large $\mathrm{Re}, \mathrm{Re}\,\mathrm{Pr}$ the evolution of the background fields due to viscosity and diffusion happens in a much longer time scale than the time scale given by the growth rate of the instabilities. In such case the evolution of the unstable modes is not expected to be affected significantly by the slow evolution of the background fields and the inclusion of S, F would not be necessary. However since the second Holmboe mode has a relatively small growth rate very large Reynolds numbers need to be considered for such an assumption to hold. In this work the inclusion of the forcing functions makes the background fields exact solutions of the Boussinesq equations (3) and (4) and allows the investigation of the instability problem free from long time scale approximations.

III. RESULTS

A. Single mode perturbations

First the evolution of a single unstable mode is examined. The size of the domain ℓ_X is chosen so that it is close to the wavelength of the fastest growing mode. For the Kelvin–Helmholtz mode ($\mathrm{Ri}=0.2$) a box of size $\ell_X = 8\pi$ was chosen and for the two Holmboe modes a box size of $\ell_x = 2\pi$.

The initial conditions for the runs consisted of the background fields given in Eqs. (1) and (2) plus a small perturbation in the velocity. A perturbation in the density field was not added because the energy of such perturbation will depend on the value of the gravitational acceleration g that is essentially varied with the Richardson number in the three examined cases. The form of the perturbation in terms of the stream function is

$$\psi_{\mathrm{pert}} = f_s(y)\sin(kx + \phi_r) + f_{as}(y)\cos(kx + \phi_r), \tag{6}$$

where ϕ_r is a random phase, k is the smallest wavenumber in the examined box, and $f_s(y)$, $f_{as}(y)$ are a symmetric and an antisymmetric functions concentrated around the mid plane

Downloaded 22 Jan 2013 to 129.199.120.226. Redistribution subject to AIP license or copyright; see http://pof.aip.org/about/rights_and_permissions

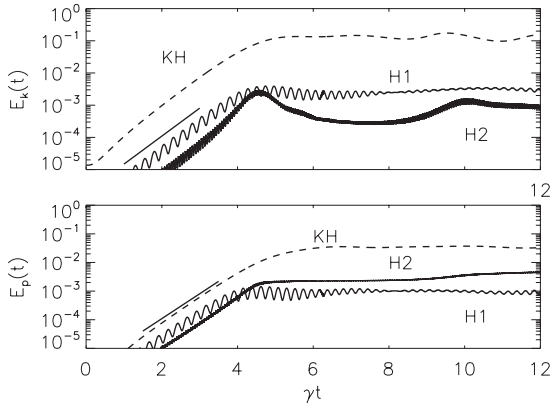

FIG. 4. Top panel: Time evolution of the kinetic energy of the perturbation of the Kelvin–Helmholtz mode dashed line (KH), the first Holmboe mode oscillating line (H1), and the H2 mode fast oscillating line (appears like thick line) (H2).

that satisfy the boundary conditions. The form of the perturbation was chosen so that there is no *a priori* exclusion of symmetric or antisymmetric solutions.

After short transient time the most unstable eigenmode becomes dominant and an exponential increase in the space averaged kinetic energy of the perturbation

$$E_k(t) = \frac{1}{\ell_X \ell_Y} \int \frac{1}{2} \rho_0 (\mathbf{u} - \mathbf{i} U_H)^2 dxdy \tag{7}$$

and the space averaged potential energy of the perturbation

$$E_p(t) = \frac{1}{\ell_X \ell_Y} \int (\rho - \rho_H) g \rho y dxdy \tag{8}$$

is observed. Figure 4 shows the time evolution of the kinetic energy E_k (top panel) and the potential energy E_p (bottom panel) of the perturbation for the three examined values of Ri in a log-linear plot. Note that since the definition of the potential energy is linear with respect to ρ the increase in the potential energy of the perturbation E_p is equal to the increase in the potential energy of the whole system. The evolution of the energy of the Kelvin–Helmholtz mode for Ri=0.2 is plotted with a dashed line and is marked as KH. The oscillating line marked as H1, corresponds to the energy of the first Holmboe mode with Ri=2.0. The fast oscillating line (that appears as a thick line) marked as H2, corresponds to the second Holmboe mode for Ri=20. The time axis has been rescaled using the growth rate γ of each mode, (obtained from the linear theory) in order to fit the three lines in one plot for comparison. As a result in the linear stage the three modes appear to grow with the same rate. The straight lines (at $1 < \gamma t < 3$) show the prediction of the linear theory $e^{2\gamma t}$. All three modes were started with the same perturbation energy, however, the Kelvin–Helmholtz mode had a shorter transient time and started growing sooner than the Holmboe modes and for this reason it appears as if the KH mode starts with more energy.

In the linear stage of evolution the energy of Kelvin–Helmholtz grows like a pure exponential $\sim e^{2\gamma t}$. Unlike the Kelvin–Helmholtz case that a single stationary mode is present Holmboe modes appear in pairs of opposite traveling waves. The observed energy evolution of the Holmboe modes shown in Fig. 4 is the energy of the sum of the two waves (left and right traveling waves) each one of which grows like $\sim e(\gamma \pm i\omega)t$. As a result the total energy scales like $\sim e^{2\gamma t}[1+\alpha \cos(2\omega t)]$ where α is a constant smaller than one that is proportional to the overlapping of the eigenfunctions of the two waves. This leads to the observed oscillations of the kinetic and potential energy in Fig. 4. The frequencies of oscillations for the first and the second Holmboe mode are similar. In Fig. 4 since the time axis has been rescaled with the growth rate the oscillations of the second Holmboe mode appear as of higher frequency. It is also worth noting that the amplitude of the oscillations of the second Holmboe mode are smaller than those for the first Holmboe mode implying that in the former case there is less overlapping of the two waves.

For γt larger than 4, the waves have reached an amplitude for which the nonlinearities become important and the exponential growth stops. The amplitude of the energy, however, that this transition occurs is very different for the three modes. In the nonlinear stage the amplitude of the kinetic energy of the KH mode is roughly two orders of magnitude bigger than that of the two Holmboe modes. The exponential growth of the first Holmboe and the second Holmboe mode stops at the same amplitude ($E_k \sim 10^{-3}$) but the evolution of the kinetic energy the second Holmboe mode is followed by a decrease in amplitude and then a subsequent rise at later times. This process appears to operate in much longer time scale than the wave crossing frequency and is possibly related to the weak coupling of two counterpropagating waves. The kinetic energy of the second Holmboe mode, however, always appears to be smaller that the kinetic energy of the first Holmboe mode roughly by a factor of 3.

The behavior of the potential energy in the nonlinear stage has a different behavior. The potential energy increase in the second Holmboe mode appears to exceed the potential energy of the first Holmboe mode. Although it is still smaller than the potential energy of the Kelvin–Helmholtz mode the difference is much smaller than that of the kinetic energy. It is worth noting that apart from the fast oscillations, on longer time scales, the potential energy is increasing monotonically this suggests that the potential energy that has been gained has been irreversibly mixed and thus cannot be returned to the flow.

The structures that develop at the nonlinear stage of evolution of the Kelvin–Helmholtz and the first Holmboe mode have been studied before in literature. Here the results of these runs are also presented for comparison with the second Holmboe mode that is examined here for the first time. Figure 5 shows the resulting structures of the Kelvin–Helmholtz instability at the nonlinear stage. The top panel shows a gray-scale image of the vorticity and the bottom panel shows a gray-scale image of the density stratification. The Kelvin–Helmholtz mode has lead to the well observed pattern where the vorticity and the density layer have rolled up. It is noted here that the snapshot that was taken at $\gamma t \simeq 6$ has already

Downloaded 22 Jan 2013 to 129.199.120.226. Redistribution subject to AIP license or copyright; see http://pof.aip.org/about/rights_and_permissions

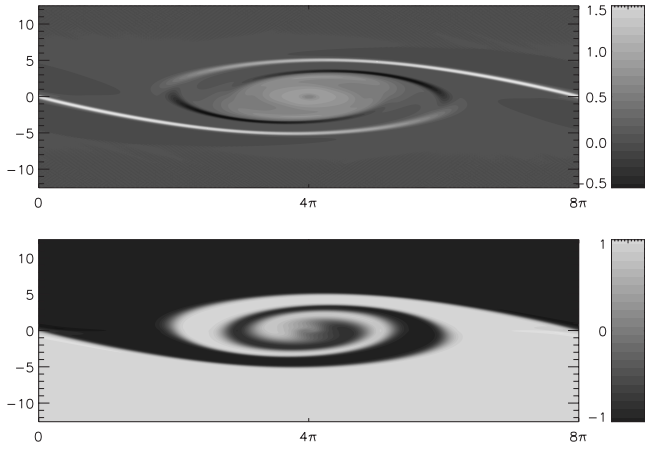

FIG. 5. Gray-scale image of the vorticity (top panel) and the density (lower panel) field at the nonlinear stage for the Kelvin–Helmholtz instability.

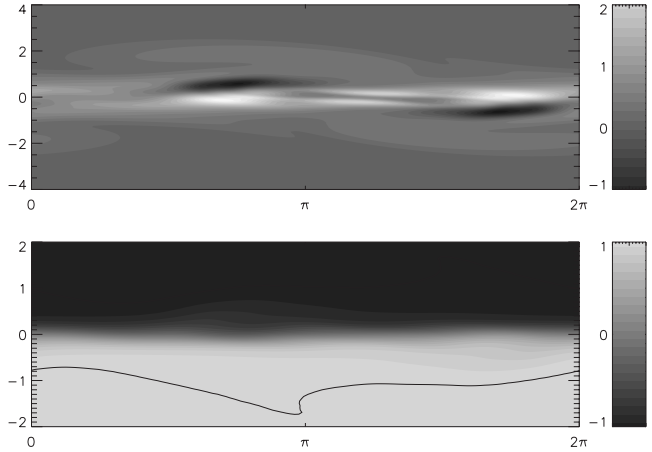

FIG. 7. Gray-scale image of the vorticity (top panel) and the density (lower panel) field at the nonlinear stage for the second Holmboe instability.

past the stage that secondary three dimensional instabilities are expected to appear if the study was in three dimensions.

Contrary to the Kelvin–Helmholtz instability the first Holmboe instability leads to a pair of gravity waves coupled with two vortices above and below the density interface that travel in opposite directions. The gravity waves form cusps and eject material and thus mix the heavy fluid below the interface with the lighter fluid on top. A snapshot of the vorticity (top panel) and density (lower panel) fields are shown in Fig. 6. The solid black lines shown in the gray-scale image of the density are the contour lines that indicate the levels that the variation of density $(\rho-\rho_0)$ has 95% of its maximum (bottom line) and minimum (top line) value.

Finally gray-scale images of the vorticity (top panel) and density (bottom panel) of the second Holmboe mode are shown in Fig. 7. The second Holmboe mode also consists of two counter propagating gravity waves. The gravity waves form cusps and mixing is the result of the breaking of these cusps just like the mechanism for mixing of the first Holmboe mode. However when comparing the structures of the first and the second Holmboe mode there are some differences that should be noted. First it can be seen that the vorticity field has a more complex structure for the second Holmboe mode that involves the coupling of two pairs of counter-rotating vortices close to the density interface. The density structures are more similar for the two modes, however, the second Holmboe mode the cusps that form in the gravity waves are much weaker and appear at higher levels of density. The density contour lines that are drawn in the lower panel of Figs. 6 and 7 indicate the levels that the variation of density $(\rho-\rho_0)$ has 99% of its maximum (bottom line) and minimum (top line) value (unlike the contour lines in Fig. 4 for the first Holmboe mode where levels of 95% was shown). This implies that for the second Holmboe mode the mixing events that are related with breaking of the cusps happen at larger heights where the density gradients are weaker and thus the mixing rate is slower.

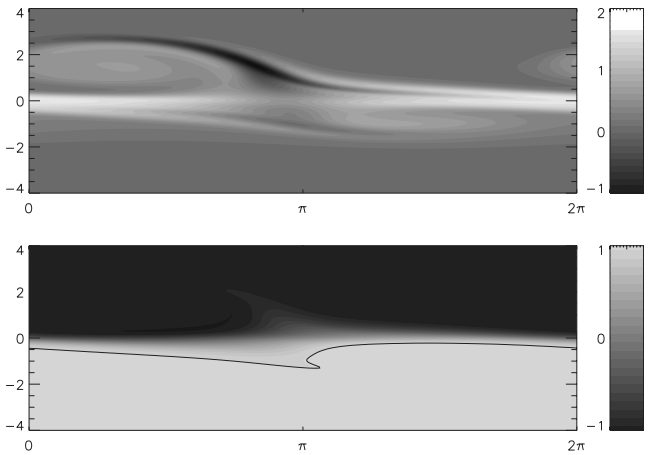

FIG. 6. Gray-scale image of the vorticity (top panel) and the density (lower panel) field at the nonlinear stage for the first Holmboe mode instability.

B. Multimode perturbation

The situation of a single mode perturbation is somehow idealistic, in more realistic situations more than one wavelength will become unstable and their coupling at the nonlinear stage could affect the resulting mixing rates. Furthermore in the previously discussed set of runs different box sizes ℓ_X were used. For a more fair comparison we need same box sizes and a more general perturbation than the excitation of just a single wavelength. For this reason a second set of runs was examined for the same Richardson numbers as in the previous subsection. Here the box width ℓ_X was set toj $\ell_X=8\pi$ for all runs. The initial perturbation in the stream function that was introduced consisted of a sum of perturbations of the form of Eq. (6) for ten wave numbers $k=2\pi n/\ell_X$ (for $n=1,\ldots,10$). The density field was left again unperturbed.

The evolution of the kinetic (top panel) and potential energy (lower panel) of the perturbation is shown in Fig. 8. Unlike Fig. 4 a linear scaling for the y-axis is used so that the nonlinear stage is more clearly displayed. However because the energy of the Kelvin–Helmholtz mode is much larger than the Holmboe modes it has been rescaled by dividing the kinetic energy by a factor of 100 and the potential energy by a factor of 10. As in Fig. 4 the time scale has been rescaled with the growth rate of each mode.

Downloaded 22 Jan 2013 to 129.199.120.226. Redistribution subject to AIP license or copyright; see http://pof.aip.org/about/rights_and_permissions

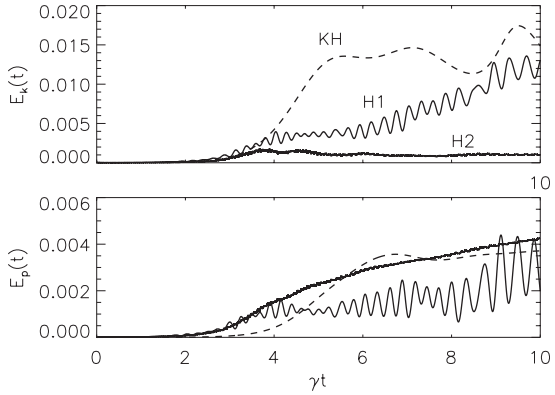

FIG. 8. The evolution of the kinetic energy (top panel) and potential energy of the perturbation for the multimode runs. The kinetic energy of the Kelvin–Helmholtz mode here shown with a dashed line and marked by KH has been decreased by a factor of 100 the potential energy has been decreased by a factor of 10. The oscillating solid line marked by H1 corresponds to the first Holmboe mode. The solid line marked by H2 corresponds to the second Holmboe mode.

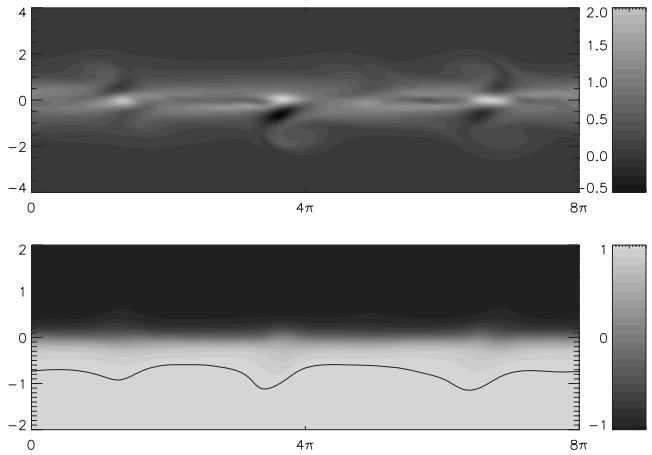

FIG. 10. Gray-scale image of the vorticity (top panel) and the density (lower panel) field at the nonlinear stage for the second Holmboe instability with $\ell_x=8\pi$.

The kinetic and potential energy of the Kelvin–Helmholtz perturbation has little difference from the previously examined case and obtains similar values of kinetic and potential energy in the nonlinear stage as with the run examined in the previous section. This is because both runs were performed in a similar size box with only the initial perturbation being changed. Only small changes were observed in the resulting structures of the vorticity and density field from the single mode run and are not shown here.

The evolution of the kinetic energy of the first Holmboe mode is shown in the top panel of Fig. 8 with the solid line marked as H1. The evolution of the two energies has similar behavior with the single mode investigations at early times. At times larger than $6<\gamma t$ there is an increase in the amplitude of kinetic and potential energy as well as an increase in the amplitude of the oscillations. This behavior is due to the coupling of the different unstable Holmboe waves. As shown in the gray-scale images of the vorticity (top panel) and density (bottom panel) of the first Holmboe mode in Fig. 9 two of the initially four vortices that had developed in the linear stage have merged leading to three vortexes below the interface and four above the interface.

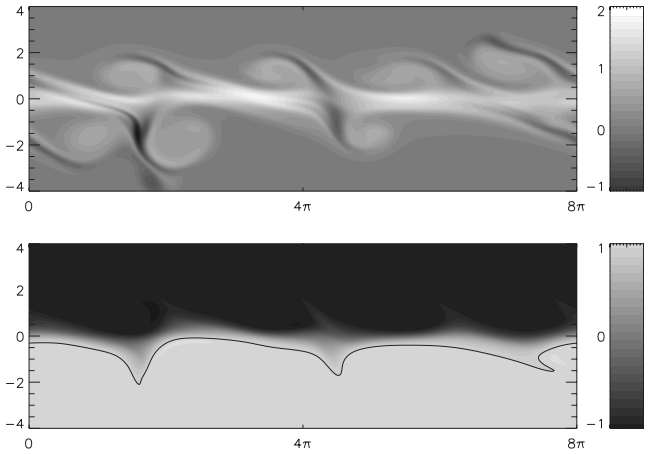

FIG. 9. Gray-scale image of the vorticity (top panel) and the density (lower panel) field at the nonlinear stage for the first Holmboe instability.

The evolution of the second Holmboe mode has also some differences than the single mode perturbation that were previously examined. First, for this run it the mode with $k=3/4$ that dominates the nonlinear behavior and not the $k=1$ as in the single mode case examined in Sec. III A. The growth rates for the two wave numbers are very similar ($\gamma=0.0156$ for $k=1$ and $\gamma=0.0150$ for $k=3/4$) and although both wave numbers were present at early times $\gamma t\sim 4$) the wave number $k=3/4$ dominated. It is also worth noting that the decrease in the kinetic energy after the first peak that was observed in the single mode run is not observed here. The potential and kinetic energies, however, have only slightly larger values than the ones observed in the single mode investigations. When compared with the first Holmboe mode the potential energy of the second Holmboe mode is larger (Fig. 10).

Finally it should be observed that there is not a clear saturated stage of the potential energy observed in the simulations. This implies that the increase of vertical mixing of mass by fluid motion has not yet been fully suppressed by the nonlinearities.

C. Prandtl number dependence

In situations that appear in nature sharp density gradients occur when the diffusion length scale is much smaller than the viscous length scale. So the validity of the assumption made in the so far presented work of unity Prandtl number is in question. In principle, high Reynolds number flows are turbulent and the molecular viscosity and diffusivity should be replaced by a turbulent viscosity and diffusivity, at this limit then the flow statistical properties will become independent of the Prandtl number. However, if such an assumption is true cannot be tested by the present (two dimensional) simulations. To address the issue of large Prandtl number a series of numerical simulations for the second Holmboe

Downloaded 22 Jan 2013 to 129.199.120.226. Redistribution subject to AIP license or copyright; see http://pof.aip.org/about/rights_and_permissions

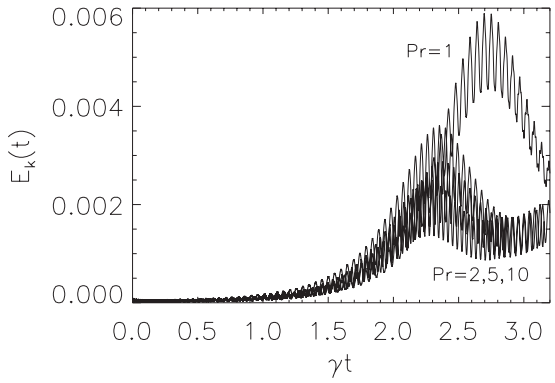

FIG. 11. Time evolution of the kinetic energy of the second Holmboe wave for four different values of the Prandtl number (Pr=1,2,5,10).

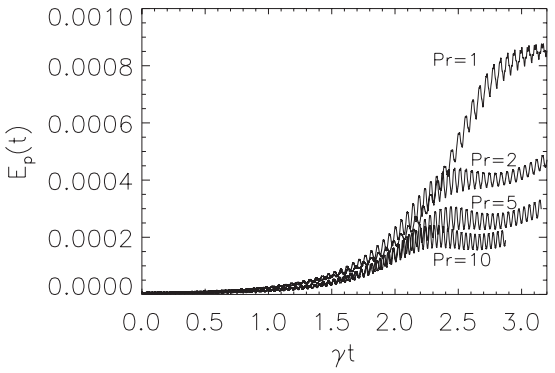

FIG. 12. Time evolution of the potential energy of the second Holmboe wave for four different values of the Prandtl number (Pr=1,2,5,10).

mode were carried out varying the Prandtl number. Four simulations are going to be presented in this section with Prandtl numbers Pr=1,2,5,10. To deal with the increasing demand for resolution as the Prandtl number is increased box sizes of half the height ℓ_Y than in Secs. III A and III B were performed and only single mode Holmboe waves were considered. Only minor differences were observed due to the box size decrease when the Pr=1 simulations were compared to the results in Sec. III B. All the other parameters in the system were kept fixed.

The simulation procedure follows exactly the same methodology as discussed in Sec. III B. The evolution of the kinetic energy of the perturbation as a function of time for four runs with different Pr (but fixed Re=500, R=4, Ri=20) is shown in Fig. 11. Although there is an initial decrease in the saturation amplitude at the nonlinear stage as the Prandtl number is increased the three runs with the largest Prandtl number (Pr=2,5,10) have very similar behavior and the three curves in Fig. 11 overlap.

The time evolution of the potential energy is shown in Fig. 12. For the potential energy a slower convergence with the Prandtl number is observed. This is however expected, since for large Pr flows diffusion mixing is suppressed, and thus also the irreversible transfer of kinetic energy to potential energy. However, in three dimensional flows and at sufficiently large Reynolds number a weaker dependence on the Prandtl number is expected. This, however, can only be addressed by three dimensional simulations.

IV. CONCLUSIONS

In this work the linear and nonlinear evolution of stratified shear flow instabilities for three different values of the Richardson number that span two orders of magnitude was investigated. The three examined values of the Richardson number correspond to three different unstable modes namely the Kelvin–Helmholtz mode for Ri=0.2 the first Holmboe mode for Ri=2.0 and the second Holmboe mode for Ri=20. All flows had identical velocity and density profiles so essentially the only parameter changed was the amplitude of gravitational acceleration.

The linear investigation of the problem has shown that the inclusion of the viscosity and diffusivity has strongly suppressed the region of instability for the two Holmboe modes that extend to arbitrary large values of the Richardson number for the inviscid problem. For the examined value of the Reynolds number Re=500 the first Holmboe mode appears only for Ri$<$7. In the range 13$<$Ri$<$30 only the second Holmboe mode is present with growth rate only three times smaller than the growth rate of the first mode at an order of magnitude smaller Ri. For strongly stratified environments therefore the higher Holmboe modes are the only modes that are able to destabilize the flow and generate turbulence at finite Re.

The nonlinear development of the three cases lead to the stretching of the density interface and enhanced mixing, however, not at the same level. From the two Holmboe modes the first mode resulted in a larger amplitude of kinetic energy in the nonlinear stage, however, the resulting potential of the second mode exceeded that of first mode. The Kelvin–Helmholtz mode was the most dominant with the kinetic energy of the perturbation reaching amplitudes hundred times bigger than that and potential energy ten times bigger than that of the Holmboe modes in much shorter times. However, if we take into account that the Richardson number has been increased by a factor of 100 a decrease in potential energy only by a factor of 10 is surprisingly small.

To summarize, in the examined parameter space and under the assumption of two dimensionality a non negligible amount of mixing and increase in potential energy is observed for values of the Richardson number much larger than unity. For larger Reynolds numbers and for three-dimensional flows the unstable flow is expected to have a better efficiency at generating small scales fast, and diffusing the advected scalars. At the same time, however, the turbulent cascade will also increase the dissipation of kinetic energy and thus decrease the ability of the flow to convert it to potential energy. So the exact dependence of the potential energy increase in the system control parameters of a realistic flow cannot be addressed in the present work, and needs to be addressed in future work. However, the results in this paper do show that the second Holmboe mode can result in finite amplitudes of kinetic and potential that can possibly lead to turbulence, even when the global Richardson number

Downloaded 22 Jan 2013 to 129.199.120.226. Redistribution subject to AIP license or copyright; see http://pof.aip.org/about/rights_and_permissions

is as large as 20. Thus it is concluded that in geophysical and astrophysical flows that are strongly stratified turbulent mixing cannot be *a priori* excluded, just by virtue of the high value of the Richardson number.

ACKNOWLEDGMENTS

I would like to thank the Laboratoire de Physique Statistique at Ecole Normale Superieure and CNRS, for hosting and supporting me during the production of this work. Some earlier computations were performed at the Observatoire de la Cote d'Azur by the IDRIS CNRS under Grant No. 070597, and SIGAMM mesocenter OCA/University Nice-Sophia and they are also thanked. Finally, I would also like to thank P. D. Mininni for his help while constructing the code.

[1] H. Luce, S. Fukao, F. Dalaudier, and M. Crochet, "Strong mixing events observed near the tropopause with the MU radar and high-resolution balloon techniques," J. Atmos. Sci. **59**, 2885 (2002).
[2] N. M. Gavrilov, S. Fukao, H. Hashiguchi, K. Kita, K. Sato, Y. Tomikawa, and M. Fujiwara, "Combined MU radar and ozonesonde measurements of turbulence and ozone fluxes in the tropo-stratosphere over Shigaraki, Japan," Geophys. Res. Lett. **33**, L09803, DOI: 10.1029/2005GL024002 (2006).
[3] D. M. Farmer and H. Freeland, "The physical oceanography of fjords," Prog. Oceanogr. **12**, 147 (1983).
[4] D. Farmer, "The flow of Mediterranean water through the Strait of Gibraltar," Prog. Oceanogr. **21**, 1 (1988).
[5] T. Oguz, E. Ozsoy, M. A. Latif, H. I. Sur, and U. Unluata, "Modeling of hydraulically controlled exchanged flow in the Bosphorous Strait," J. Phys. Oceanogr. **20**, 945 (1990).
[6] S. Yoshida, M. Ohtani, S. Nishida, and P. F. Linden, in *Physical Processes in Lakes and Oceans*, edited by J. Imberger (American Geophysical Union, Washington, DC, 1998).
[7] R. Rosner, A. Alexakis, Y. Young, J. Truran, and W. Hillebrand, "On the C/O enrichment of novae ejecta," Astrophys. J. Lett. **562**, L177 (2002).
[8] A. Alexakis, A. C. Calder, A. Heger, E. F. Brown, L. J. Dursi, J. W. Truran, R. Rosner, D. Q. Lamb, F. X. Timmes, B. Fryxell, M. Zingale, P. M. Ricker, and K. Olson, "On heavy element enrichment in classical novae," Astrophys. J. **602**, 931 (2004).
[9] P. Garaud, "Latitudinal shear instability in the solar tachocline," Mon. Not. R. Astron. Soc. **324**, 68 (2001).
[10] B. Galperin, S. Sukoriansky, and P. S. Anderson, "On the critical Richardson number in stably stratified turbulence," Atmos. Sci. Lett. **8**, 65 (2007).
[11] S. S. Zilitinkevich, T. Elperin, N. Kleeorin, and I. Rogachevskii, "Energy- and flux-budget (EFB) turbulence closure model for stably stratified flows. Part I: Steady-state, homogeneous regimes," Boundary-Layer Meteorol. **191**, 125 (2007).
[12] S. S. Zilitinkevich, T. Elperin, N. Kleeorin, I. Rogachevskii, I. Esau, T. Mauritsene, and M. W. Miles, "Turbulence energetics in stably stratified geophysical flows: Strong and weak mixing regimes," Q. J. R. Meteorol. Soc. **134**, 793 (2008).
[13] S. P. Hazel, "Numerical studies of the stability of inviscid shear flows," J. Fluid Mech. **51**, 3261 (1972).
[14] L. N. Howard, "A note on a paper of John Miles," J. Fluid Mech. **10**, 509 (1961).
[15] Lord Kelvin, "Influence of wind and capillarity on waves in water supposed frictionless," *Hydrodynamics and General Dynamics*, Mathematical and Physical Papers (1910), Vol. 4, p. 76.
[16] H. Helmholtz, "Uber discontinuirliche Flüssigkeitsbewegungen," Wissenschaftliche Abhandlungen **3**, 146 (1868).
[17] J. Miles, "On the stability of heterogeneous shear flow Part 2," J. Fluid Mech. **16**, 209 (1963).
[18] S. A. Thorpe, "Turbulence in stably stratified fluids: A review of laboratory experiments," Boundary-Layer Meteorol. **5**, 95 (1973).
[19] S. A. Thorpe, "A method of producing a shear flow in a stratified fluid," J. Fluid Mech. **32**, 693 (1968).
[20] C. P. Caulfield and W. R. Peltier, "Three dimensionalization of the stratified mixing layer," Phys. Fluids **6**, 3803 (1994).
[21] A. B. Cortesi, G. Yadigaroglu, and S. Banerjee, "Numerical investigation of the formation of three-dimensional structures in stably-stratified mixing layers," Phys. Fluids **10**, 1449 (1998).
[22] W. D. Smyth, "Dissipation-range geometry and scalar spectra in sheared stratified turbulence," J. Fluid Mech. **401**, 209 (1999).
[23] C. Staquet, "Mixing in a stably stratified shear layer: two- and three-dimensional numerical experiments," Fluid Dyn. Res. **27**, 367 (2000).
[24] W. D. Smyth, J. N. Moum, and D. R. Caldwell, "The efficiency of mixing in turbulent patches: Inferences from direct simulations and microstructure observations," J. Phys. Oceanogr. **31**, 1969 (2001).
[25] C. P. Caulfield and W. R. Peltier, "The anatomy of the mixing transition in homogeneous and stratified free shear layers," J. Fluid Mech. **413**, 1 (2000).
[26] W. R. Peltier and C. P. Caulfield, "Mixing efficiency in stratified shear flows," Annu. Rev. Fluid Mech. **35**, 135 (2003).
[27] G. P. Klaassen and W. R. Peltier, "The influence of stratification on secondary instability in free shear layers," J. Fluid Mech. **227**, 71 (1991).
[28] W. D. Smyth and W. R. Peltier, "The transition between Kelvin–Helmholtz and Holmboe instability: An investigation of the over-reflection hypothesis," J. Atmos. Sci. **46**, 3698 (1989).
[29] J. Holmboe, "On the behaviour of symmetric waves in stratified shear layers," Geofys. Publ. **24**, 67 (1962).
[30] W. D. Smyth, G. P. Klaasen, and W. R. Peltier, "Finite amplitude Holmboe waves," Geophys. Astrophys. Fluid Dyn. **43**, 181 (1988).
[31] W. D. Smyth and W. R. Peltier, "Instability and transition in finite amplitude Kelvin–Helmholtz and Holmboe waves," J. Fluid Mech. **228**, 387 (1991).
[32] B. R. Sutherland, C. P. Caulfield, and W. R. Peltier, "Internal gravity wave generation and hydrodynamic instability," J. Atmos. Sci. **51**, 3261 (1994).
[33] W. D. Smyth and K. B. Winters, "Turbulence and mixing in Holmboe waves," J. Phys. Oceanogr. **33**, 694 (2003).
[34] J. R. Carpenter, G. A. Lawrence, and W. D. Smyth, "Evolution and mixing of asymmetric Holmboe instabilities," J. Fluid Mech. **582**, 103 (2007).
[35] W. D. Smyth, "Secondary circulations in Holmboe waves," Phys. Fluids **18**, 064104 (2006).
[36] W. D. Smyth, J. R. Carpenter, and G. A. Lawrence, "Mixing in symmetric Holmboe waves," J. Phys. Oceanogr. **37**, 1566 (2007).
[37] F. K. Browand and C. D. Winant, "Laboratory observations of shear layer instability in a stratified fluid," Boundary-Layer Meteorol. **5**, 67 (1973).
[38] G. A. Lawrence, F. K. Browand, and L. G. Redekopp, "The stability of a sheared density interface," Phys. Fluids A **3**, 2360 (1991).
[39] O. Pouliquen, J. M. Chomaz, and P. Huerre, "Propagating Holmboe waves at the interface between two immiscible fluids," J. Fluid Mech. **266**, 277 (1994).
[40] C. P. Caulfield, W. R. Peltier, S. Yoshida, and M. Ohtani, "An experimental investigation of the instability of a shear flow with multi-layered density stratification," Phys. Fluids **7**, 3028 (1995).
[41] G. Pawlak and L. Armi, "Vortex dynamics in a spatially accelerating shear layer," J. Fluid Mech. **376**, 1 (1998).
[42] D. Z. Zhu and G. A. Lawrence, "Holmboe's instability in exchange flows," J. Fluid Mech. **429**, 391 (2001).
[43] A. M. Hogg and G. N. Ivey, "The Kelvin–Helmholtz to Holmboe instability transition in stratified exchange flows," J. Fluid Mech. **477**, 339 (2003).
[44] M. E. Negretti, D. Z. Zhu, and G. H. Jirka, "Barotropically induced interfacial waves in two-layer exchange flows over a sill," J. Fluid Mech. **592**, 135 (2007).
[45] A. Alexakis, "On Holmboe's instability for smooth shear and density profiles," Phys. Fluids **17**, 084103 (2005).
[46] A. Alexakis, "Marginally unstable Holmboe modes," Phys. Fluids **19**, 054105 (2007).
[47] P. G. Drazin and W. H. Reid, *Hydrodynamic Stability* (Cambridge University Press, Cambridge, England, 1981).
[48] R. Courant, K. Friedrichs and H. Lewy "Uber die partiellen Differenzengleichungen der mathematischen Physik," Math. Ann. **100**, 32 (1928).
[49] S. Ortiz, J.-M. Chomaz, and T. Loiseleux, "Spatial Holmboe instability," Phys. Fluids **14**, 2585 (2002).
[50] A. Yu. Gelfgat and E. Kit, "Spatial versus temporal instabilities in a parametrically forced stratified mixing layer," J. Fluid Mech. **552**, 189 (2006).

Downloaded 22 Jan 2013 to 129.199.120.226. Redistribution subject to AIP license or copyright; see http://pof.aip.org/about/rights_and_permissions